

Macrobending SMS fiber-optic anemometer and flow sensor

Jesse W. Costa^{a,*}, Marcos A.R. Franco^b, Valdir A. Serrão^b, Cristiano M.B. Cordeiro^c,
Maria T.R. Giraldi^{d,*}

^a Centro Federal de Educação Tecnológica Celso Suckow da Fonseca – CEFET-RJ, Rio de Janeiro, RJ, Brazil

^b Instituto de Estudos Avançados – IEAv, São José dos Campos, SP, Brazil

^c Instituto de Física Gleb Wataghin, UNICAMP, Campinas, SP, Brazil

^d Instituto Militar de Engenharia – IME, Rio de Janeiro, RJ, Brazil

ARTICLE INFO

Keywords:

Fiber-optic sensor
Single mode-multimode-single mode structure
Multimodal interference
Bend
Flow sensor
Anemometer

ABSTRACT

We report a simple, high sensitivity, good resolution and low-cost fiber-optic anemometer and flow sensor based on reflective single mode-multimode-single mode structure bent by air flow. The dragging force on the multimode section causes it to bend resulting in multimodal interference (MMI) effects which are related to the fluid velocity and flow rate. Bending effects on the output power profile are investigated and numerical simulation combined with experimental data demonstrate that the output power intensity may increase or decrease with the rise of curvature, depending on MMI conditions and field deformation. The sensor behavior with air flow velocity is evaluated by spectral analysis using a variety of methods as wavelength shifting of a selected peak and output power intensity of selected wavelength and output power intensity of selected points. Experimental tests using air stream inside a wind tunnel provided a reliable dynamic range from 4 to 10 m/s. Peak sensitivities of 435.13 pm/(m/s) with resolution of 17.4×10^{-3} m/s for wavelength shifting and 2.62 dB/(m/s) for output power intensity are obtained. These results assure that the sensor can be effectively used in a wide variety of applications, such as anemometer and flow rate meter.

1. Introduction

Several interferometric devices [1–4] have been investigated in order to develop optical fiber sensors for physical parameters such as temperature, refractive index, vibration, strain, bending and displacement [5–10]. Most of them use multimodal interference (MMI) in a well-known single mode-multimode-single mode (SMS) optical structure [7–9]. Some SMS based sensors use Mach-Zehnder interferometry as in [10] where an air gap is added before the last single-mode section for displacement sensing. Some SMS structures use interference of a few modes which allows the generation of microwaves in the 100 GHz region [11]. In [12] a SMS structure interferometer using curvature variation allows the generation of 100 GHz free spectral range (FSR) multi-wavelength laser with FSR tuning capabilities.

Numerous techniques involve optical fiber bend sensing for diverse sensors purposes like vibration [7,9], wavelength variation for bending sense [13], curvature and strain sensing using suspended multicore fiber [14], displacement using high bend loss single mode fiber [15], load using a variation of the number of bends [16] and evanescent wave using hetero-core structure as macrobend sensor [17].

Various investigated flow sensors use diverse techniques. Some use

light coupling where sensor displacements caused by the flow stream produce misalignment between the light transmitter and receiver [18–20]. Michaelson interferometer is reported in [21] using a twin-core fiber as flow velocity sensor. Doppler shift of scattered radiation of a single mode semiconductor laser employing a fiber-optic probe is used in [22] for blood flow sensing. Fiber bending loss produced due to flow stream is used in [23], where a bending probe with a square block fastened to it by a thin wire line is dragged by the flow altering the transmitted power. A cantilever structure is used in [24] in order to produce the bending effect. Another cantilever bending structure is employed in [25] to detect the air-gap changes from two fiber sensors caused by the bending of the cantilever beam using the strain principle, as a result of the flow stream. A Fabry-Perot cavity is used in [26] to measure water flow. A fiber-optic anemometer with temperature self-compensation using Fabry-Perot interferometer is described in [27]. A variety of Fiber Bragg Gratings (FBG) devices used as flow sensors are described in [28–31]. A fiber-optic mass flow sensor based on Coriolis force is reported in [32]. In [33] a water wave gauge is described. It uses a transmission type SMS structure where the multimode section is free to move with the wave frequency. A reflection type sensor where a LED light is transmitted and reflected back to be received by a photo

* Corresponding authors.

E-mail addresses: jjcesse@gmail.com (J.W. Costa), mtmrocco@ime.ub.br (M.T.R. Giraldi).

detector is described in [34]. In this structure a number of steps-like grooves on the cladding of the fiber are responsible for a higher reduction in light intensity when the fiber is bent due to flow stream at the particular region.

This work proposes an optical fiber SMS-MMI reflective bend sensor that can be used as flow sensor and anemometer. The structure is basically a single mode fiber (SMF) used simultaneously as input and output fiber spliced with a segment of multimode fiber (MMF) with a gold film coated on its end face. The MMF section is placed into an air flow stream across the fiber which imposes a transverse force causing it to bend resulting in MMI effects which are related to the fluid velocity and flow rate. MMI self-image condition is used to allow higher output power evaluation, since the input light power is nearly replicated at this point. Fluid flow in pipes is commonly encountered in practice and presents many residential, commercial and industrial applications. Hot or cold water, oil and also gases are common examples of pipe use in industrial plants and inside machines. Flow sensors placed inside a pipe give essential information concerning fluid flow properties like fluid velocity and flow rate. Among many advantages of the proposed fiber flow sensor, we can point out its electromagnetic immunity, resistance to corrosion, ability to measure reverse flow and, as it virtually doesn't create obstruction to flow, there is no pressure loss. In free air and many other air velocity measurements the structure can be used to measure wind velocity as an anemometer. It includes other application possibilities like in aeronautics, for instance, as an indicator of stall if placed in aerodynamic surfaces of airplanes.

In Section 2 the basic principles of the SMS sensor are presented including SMF-MMF coupling factors and the self-image condition. In Section 3 the MMI bend effects on the output power profile are discussed. Experimental measurements and numerical simulation were implemented to certify that behavior. The bending sensor and flow sensing mechanism are described in Section 4 along with the experimental setup, which includes the use of a wind tunnel to confirm the bending effects on flow sensing. In Section 5 experimental results are discussed and the speed and flow rate association with the sensor output power profile and spectral peak shifting are investigated. In Section 6 the conclusions are exposed due to the utilization of the proposed sensor as anemometer and flow sensor.

2. Basic principles

SMS is typically an optical configuration obtained by splicing a MMF fiber segment between two SMF segments as shows in Fig. 1. The electromagnetic field from a light source propagated in the SMF segment is coupled to several modes into the MMF section and the multimode interferometry implies a pattern of successive constructive and destructive interferences along the fiber. At the end of the MMF segment the light is coupled to the last SMF section and the coupling efficiency depends on the amplitudes and relative phases of the several modes at the exit end of the MMF.

Though multimode fibers can hold a very large number of modes, not all of them are excited in the SMF-MMF coupling interface and the excited ones are not excited the same way [3,35]. The power

distribution among the excited modes has direct influence on the output power profile for a SMS bend sensor as the individual mode contributions to the total output power have their own specific behavior as a function of bending. The lower order modes are more internal or paraxial at the input of the MMF section and at the self-image region as well. They also usually hold the higher amount of power. This feature means that, for the output power, lower order modes are less sensitive to bending for high values of curvature radius but very sensitive for very low curvature radius. It is possible to determine the amount of the input field power that couples to each specific mode in the MMF using the well-known power coupling coefficient given by the overlap integral of that field and the field distribution at the MMF [35]. As the input field does not contain any azimuthal components, the representation for the field inside the MMF is a sum of radial linearly polarized modes.

The several $LP_{0\nu}$ excited modes, where ν is the mode number, interfere mutually as the light propagates along the MMF. The phase difference $\Delta\phi_{mn}$ between two modes, LP_{0m} and LP_{0n} , after propagating a determined distance can be expressed as [3]

$$\Delta\phi_{mn} = (\beta_m - \beta_n) \cdot 2L_p = \frac{\lambda(u_m^2 - u_n^2)}{4\pi a^2 n_{core}} \cdot 2L_p = N\pi \quad (1)$$

where β_m and β_n are the longitudinal propagation constants for the modes m and n , L_p is the propagation distance, $u_m = \pi(m - 1/4)$ and $u_n = \pi(n - 1/4)$ are the roots of the Bessel function of zero order, a is the radius of the MMF core, n_{core} is the refractive index of the MMF core and N is a integer number. The wavelength for a constructive (when N is an even number) or a destructive (when N is an odd number) interference can be expressed as [3]

$$\lambda = \frac{8a^2 n_{core} N}{(m - n)[2(m + n) - 1]L_p} \quad (m > n) \quad (2)$$

A periodic condition found along the direction of propagation where field condensation occurs due to constructive interference among the guided modes leads to the self-imaging effect where the light field at the input of the MMF section is nearly reproduced at a well-defined propagation distance for a specific wavelength in both amplitude and phase [35,36]. The base condition is that the guided modes interfere with the same relative phases, in constructive interferences. As described in [35], the first self-image distance from the MMF light input is given by

$$Z_{self-imaging} = \frac{4n_{core}d^2}{\lambda} \quad (3)$$

It depends on the refractive index of the fiber core n_{core} , its diameter d and the wavelength of the light source λ . The application described in this work rely on MMI effects combined with self-imaging conditions. A self-image length of nearly 41.21 mm at 1.546 μ m wavelength was obtained with Eq. (3) using SMF standard Corning SMF-28 and MMF Thor Labs 105/125 μ m ($n_{core} = 1.4446$, $n_{clad} = 1.4271$).

3. Bending effect on the output power profile

The behavior of the SMS bend sensor output power intensity as a function of the curvature radius is directly associated to the power distribution in the MMF excited modes and how they interfere as a function of bending. Total power at the SMS output depends on the constructive and destructive interferences in amplitude and phase caused by each separate mode and the resulting effect is the sum of the contributions. At first impression it may seem that the total output power will lower with the rise of curvature, or reduction of the curvature radius, due to loss attenuation. This is not totally true. The output power profile as a function of the curvature radius has alternate slopes since the contributions of each mode to the constructive and destructive interferences along the propagation vary with the bending

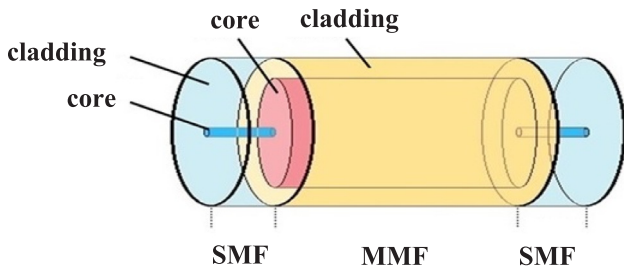


Fig. 1. SMS general structure.

radius, which changes the transverse energy distribution in a manner that in some ranges the output power increases when the bending radius increases while in others it has the opposite behavior. Another contribution to this behavior is the field deformation caused by curvature. The fields in low order modes may be changed by curvature and so may the losses, as depicted in [37], since it shifts away from the axis in the direction opposite to the center of curvature and narrows as it shifts. The losses of modes that are deformed by curvature actually decrease if the narrowing effect happens. Wide fields are more susceptible to curvature loss than narrow field distributions [37].

Each mode has its specific response to bending, since each one has its own coupled power, amplitude and phase contributions, with its effective propagation index. The lower order modes are more paraxial at the self-image region and, therefore, less sensitive to high curvature radius bending, which is the opposite behavior of the higher order modes which are more external [38]. One cannot expect that amplitude and phase will match the same way among several propagating modes as the fiber enhances its curvature. Thereupon the sum of the contributions is not linear and does not increase continuously with bending radius.

Experimental tests were made to confirm this alternating slope behavior. Fig. 2(a) shows the experimental setup built to measure the transmitted light power through a SMS sensor as a function of the bending radius. The bending effect was accomplished using a micro positioner with resolution of 10 μm . The sensor was placed at half

distance between the two posts and the curvature, which is the inverse of the curvature radius, is given by [39],

$$C = \frac{1}{R} = \frac{2h}{h^2 + (d/2)^2} \quad (4)$$

$$d = L_0 - \Delta L \quad (5)$$

where h is the depth of the curvature, L_0 is the initial distance and ΔL is the distance variation. For small lengths of h , which makes it difficult to be measured, Eq. (4) can be approximated by [7]

$$C = \frac{1}{R} \cong \frac{4}{L_0} (L_0^2 - d^2)^{\frac{1}{2}} \quad (6)$$

The experimental results of the bending sensor are shown in Fig. 2(b), where the output power profile is obtained for a wide range of bending radius. The light source was a narrow band laser centered at $\lambda = 1.546 \mu\text{m}$.

Numeric tools were also employed to simulate the transmission profile of the SMS sensor. The results obtained with commercial beam propagation method simulation software using the same wavelength of 1.546 μm are also shown in Fig. 2(b). As can be seen from the results, the transmission profile slopes alternate in both experimental and simulated evaluations with a good agreement. Clearly the output power does not increase continually as the curvature radius increases. Both results in Fig. 2(b) show the output power normalized by the input light power. Some additional attenuations sources are expected to be present at the experimental tests, which leads to lower values.

4. Flow sensing principle and experimental setup

The SMS structure used in the flow sensing experiment is shown in Fig. 3(a). The sensor uses a reflective structure which is basically a single mode fiber used simultaneously as input and output fiber spliced with a segment of multimode fiber with a gold film coated on its end face. This bending sensing structure uses the SMF Corning SMF-28 spliced to the MMF Thorlabs 105/125 μm with half the length of the self-image since the light is reflected back at the gold film.

A schematic diagram of the experimental setup is shown in Fig. 3(b). The light emitted from a wideband source (Thorlabs Fiber Coupled SLD 1550 nm which provided a 1450–1650 nm band) is guided into the sensor through a circulator and the interrogator is a portable field applications OSA JDSU with wavelength range of 1250–1650 nm and resolution of 7.57 pm. For applications in flow sensing, the principle is to use the MMF section as a cantilever beam sticking freely out in the fluid stream across the fiber which imposes a transverse dragging force causing it to bend, resulting in MMI effects which are related to the fluid speed. It is also possible to use some sort of frontal protection to the fiber in order to prevent damage or breakage, especially at the

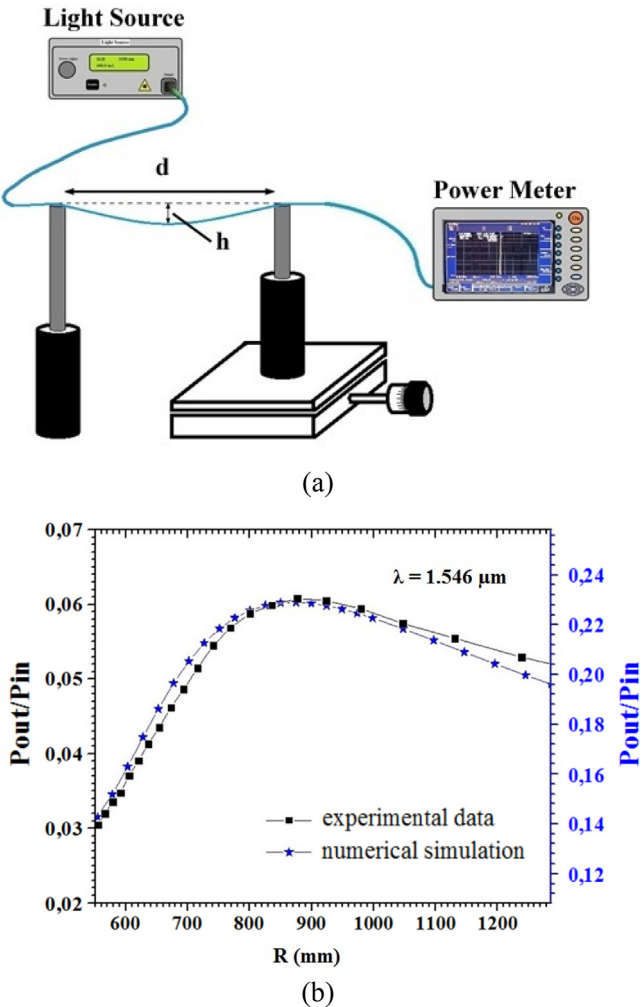


Fig. 2. (a) Experimental setup to measure the bending characteristic of the SMS sensor and (b) experimental (left scale) and numerical simulation results. The output power scales are normalized by the input light power.

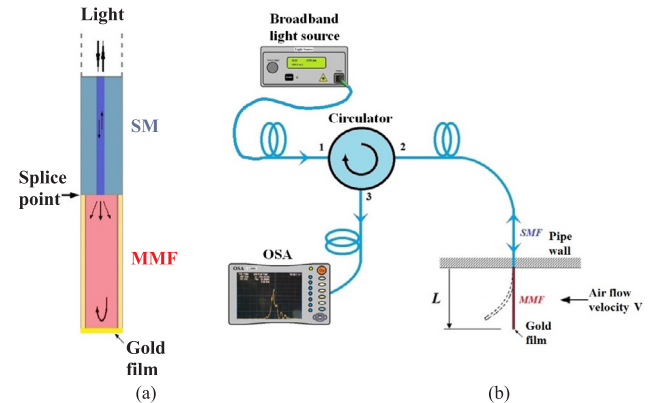


Fig. 3. (a) SMS fiber optic sensor using coated gold film in order to reflect the light and (b) schematic diagram of the experimental setup.

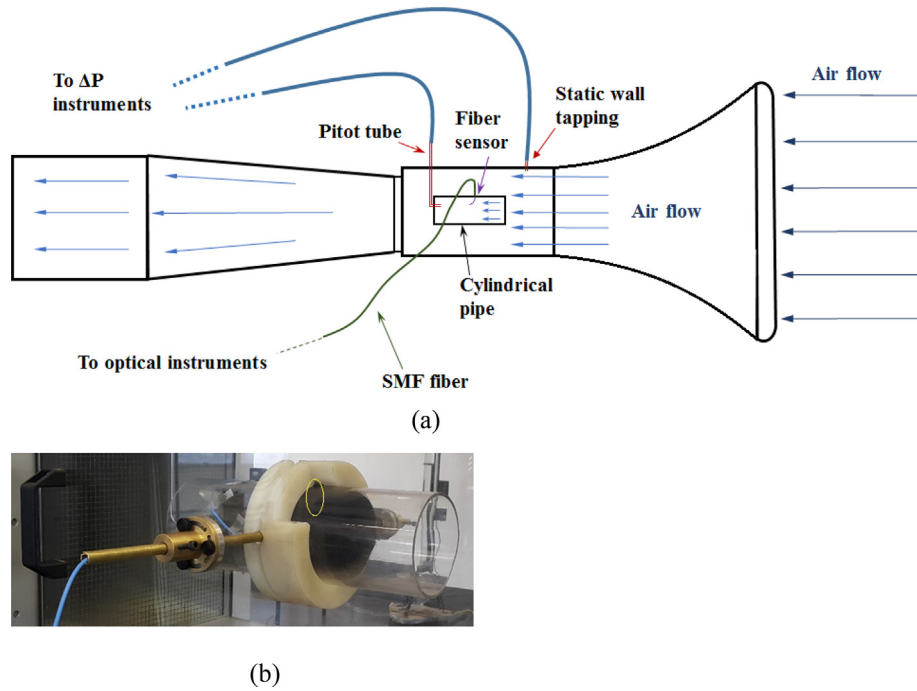


Fig. 4. (a) Wind tunnel setup layout and (b) Sensor mounting at the acrylic tube with associated hardware inside the test chamber (the yellow ellipse shows the position of the sensor inside the tube) at Unicamp University.

splice region, depending on the nature and speed of the fluid.

Experimental tests evaluated the sensor behavior in a wind tunnel (TecQuipment AF100 Subsonic Wind Tunnel) and, therefore, the moving fluid is air flow. The fiber sensor was mounted inside a 94 mm internal diameter acrylic tube in order to avoid the influence of the mounting hardware in the air stream flow at the sensor position. The general wind tunnel setup and the detail of the tube mounting with associated hardware in the test chamber are shown in Fig. 4(a) and (b), respectively. The wind tunnel has pitot tubes to measure the static and stagnation pressure inside the test chamber in order to give differential dynamic pressure in mmH₂O which leads to the velocity of the air flow. The pitot tubes were positioned to measure the velocity of the air at the sensor level.

Using Bernoulli equation, the relation between differential dynamic pressure and air velocity is given by,

$$V = \sqrt{\frac{19.62\Delta P}{\rho_a}} \quad (7)$$

$$\rho_a = \frac{100P_a}{RT_a} \quad (8)$$

where V is the velocity in m/s, ΔP is the differential dynamic pressure in mmH₂O, ρ_a is the local air density in kg/m³, T_a is the ambient air temperature in K, P_a is the ambient atmospheric pressure in mbar and R is the gas constant (287 m²/s²K). The column of water that indicates the pressure is graded in units of mmH₂O, which leads to an uncertainty of 0.5 mmH₂O. Using the relations stated in Eqs. (7) and (8), the range of differential pressure measurements taken in the experimental tests from 0 (no wind) to 9 mmH₂O is related to air velocity range from 0 to 12.25 m/s.

Through a circulator the light reaches the OSA as shown in Fig. 3(b). The light power received at the MMF-SMF interface after the reflection at the MMF end face with gold film depends on the MMI along the MMF segment which is a function of its length L , which is chosen to be the half (due to the reflection arrangement) of the self-image condition given by Eq. (3). Experimental limitations concerning the fabrication of the sensor and the assembly of the sensor set at the acrylic tube and wind tunnel led to a small variation in the resulting peaks of light power

in the spectrum of the straight fiber (no wind), which may lead to different detected peak wavelengths. According to Eq. (3), it implies that the effective length of the MMF section is different than calculated at $\lambda = 1.546 \mu\text{m}$ and the power output is, consequently, lower than the expected at the self-image position. Depending on the MMI conditions among the guided modes and also fields displacements [36], it is possible to obtain higher output light power as the sensor bends with the stream flow if it leads the output light closer to the self-imaging condition.

5. Experimental results and discussions

The experiment was conducted using air flow through an acrylic circular tube in the test chamber of the wind tunnel, as shown in Fig. 4. Studies of internal flow in circular long pipes describe a hydrodynamic entrance region which starts at the pipe entrance and goes up to the point where begins the fully developed zone. In this region the laminar flow provided by the wind tunnel in the test chamber assumes the permanent behavior along the pipe, which depends on the Reynolds number. That behavior would be turbulent, considering the properties of the air flow in the tube used in the experiment. Since the sensor position inside the tube is half of its length and the tube is very much shorter than the length of the hydrodynamic entrance region, the air flow can be considered as to be laminar with very good approximation and we can assume that the flow rate Q can be calculated simply by multiplying the air speed V by the area A of the tube cross-section as,

$$Q = V \cdot A = V \cdot \pi \cdot r^2 \quad (9)$$

where r is the internal radius of the tube.

The reflecting spectra measured in the experiment for different established dynamic pressure, with the corresponding velocities, is shown in Fig. 5. It contains several peaks and valleys due to multimodal interference effects. P1, P2, and V1 were chosen among them to illustrate the main sensor properties, by tracking their intensity or position changes along the spectral evolution with the dynamic pressure.

Table 1 shows the experimental wavelength values λ_{exp} found for the selected points in the reflected spectra with no bend curvature, namely air flow velocity zero, together with the calculated values λ_{calc}

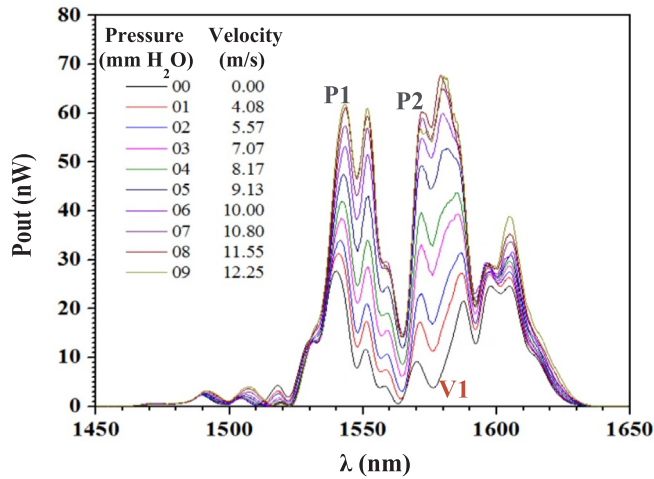


Fig. 5. Experimental reflection spectra of the SMS sensor at different air flow velocities. Peaks P1 and P2 and valley V1 are selected to illustrate the main sensor properties.

Table 1

Calculated and experimental wavelengths of interferences for a pair of modes m and n .

Peak/Valey	m,n	N	$\Delta\lambda_{\text{calc}}$ (nm)	λ_{calc} (nm)	λ_{exp} (nm)
P1	9,2	292	5.27483	1540.25	1539,93
	9,3	274	5.61884	1539.56	
P2	7,3	154	10.20263	1571.21	1570,25
	9,1	308	5.10132	1571.21	
V1	5,3	61	25.84667	1576.65	1576,23
	9,1	309	5.10132	1576.31	
Experimental values:	$l_{\text{p}(\text{exp})}$	n_{core}	a 52.5 μm		
	41.08 mm	1.4446			

using Eq. (2). The $\Delta\lambda_{\text{calc}}$ values is the spacing between the interferences, calculated with $N = 1$ (due to first phase difference between two modes LP_{0m} and LP_{0n}) in Eq. (2). In the λ_{calc} column we consider the interference effect between different pairs of modes (m,n) and calculate the corresponding wavelengths for the selected peaks and valley, which have good agreement with experimental values.

As can be depicted from Table 1, peak P1 is dominated by the constructive interferences among (LP_{09} and LP_{02}) and (LP_{09} and LP_{03}) mode pairs, P2 is dominated by the constructive interferences among (LP_{07} and LP_{03}) and (LP_{09} and LP_{01}) and V1 is dominated by the destructive interferences among (LP_{05} and LP_{03}) and (LP_{09} and LP_{01}). Therefore, the main difference on the output power between peaks P1 and P2 relies on the difference of energy transferred from the SMF to the MMF and then back to the SMF by the constructive interference between the mode pairs (9,2 and 9,3) and (7,3 and 9,1).

The mode pairs 9,2 and 9,3 together are responsible for higher light energy coupled from the SMF segment to the MMF section of the sensor, than the light energy coupled by the mode pairs 7,3 and 9,1. Referring to the sensor in still state, namely not bent, represented by the black curve in Fig. 5, the peak P1 actually has higher output power than P2, as expected. The modal comparison between P2 and V1 is that the difference relies in the modal components LP_{05} (V1) and LP_{07} (P2). V1 has a higher energy modal component, but its interference is destructive. Some minor contributions can also produce influence on the peaks, but the referred mode pairs are responsible for the main effects.

Fig. 6 shows the wavelength shift as a function of the air velocity for the selected points. The lines are only considered to observe a general tendency of the wavelength shift as a function of the bending. A more precise discussion about the sensor sensitivity will take place later on this section. The wavelength of valley V1, which is a result from the interference among (LP_{05} and LP_{03}) and (LP_{09} and LP_{01}) pairs of modes,

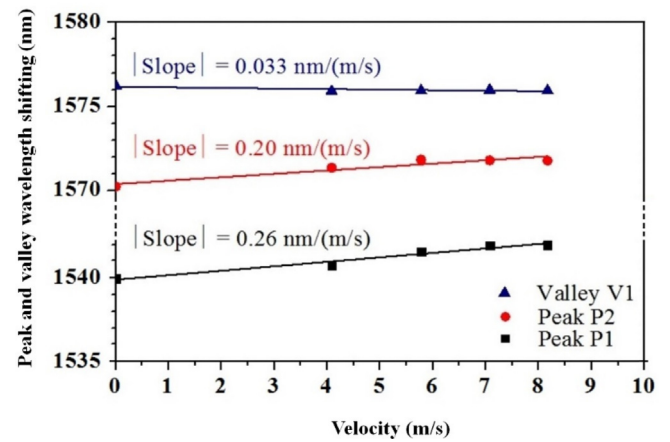


Fig. 6. Wavelength shift of the selected points P1, P2 and V1.

remains almost constant. The modal composition of V1 is more paraxial comparing to the others, which means more focused within a smaller area near the fiber core center and therefore it is less affected by the bending effect for low curvature, as in the case reported here. It is expected to be very sensible for very high curvatures, namely very low curvature radius. Peaks and valleys that are less sensitive to the curvature changes offer the possibility to measure simultaneously another parameter like temperature. The higher order mode pairs (LP_{09} and LP_{02}) and (LP_{09} and LP_{03}) of P1 are more affected by the bending effect for low curvature, indicating higher sensitivity in the small curvature range. As P2 is dominated by the mode pairs (LP_{07} and LP_{03}) and (LP_{09} and LP_{01}), it has an intermediate behavior regarding the wavelength shift effect.

Fig. 7(a) shows the wavelength shift of P1 peak as a function of the dynamic pressure. Since the resolution of the pressure measurement instrument is 1 mm, the uncertainty is considered to be 0.5 mm, namely the half of the resolution. The uncertainty for the wavelength is negligible as the OSA resolution is in the order of few pm. A polynomial fit of order 2 is shown as a solid line. Fig. 7(b) shows the wavelength shift of P1 peak as a function of the air flow velocity (bottom scale) and the corresponding air flow rate (top scale), converted using Eqs. (7)–(9). As the error bars of pressure converted to velocity using Eqs. (7) and (8) have no symmetry, the fitting function of Fig. 7(a) was converted, in order to fit velocity and flow rate, using the same Eqs. (7)–(9). Fig. 7(c) shows the sensitivity of the sensor.

The sensor experiment with no air flux results in dynamic pressure zero and so the air velocity and flow rate. Increasing the air flux to the first degree of the pressure instrument scale, namely 1 mmH₂O, the corresponding air velocity is 4.08 m/s. Therefore, the measurements provided no information concerning very low air flow velocities. As a consequence, the results in Fig. 7 bring no true meaning for the peak shift as a function of pressure, air velocity or flow rate at the region of very low velocity (less than 4 m/s). A similar behavior shall be considered at high velocity values region (greater than 10 m/s) due to some saturation of the sensor displacement with the dragging force of the air flow. At this point the sensor was bent to displacement limit and the measurements are not expected to be reliable. The best consistent behavior of the sensor is to be expected nearly in the range from 4 to 10 m/s. At the lower limit of 4 m/s and higher limit of 10 m/s the sensitivity is nearly 330.71 pm/(m/s) and 304.40 pm/(m/s), respectively. A peak sensitivity of 435.13 pm/(m/s) happens nearly the center of the chosen region (4 to 10 m/s), namely 7.05 m/s. At this range the average sensitivity is 405.50 pm/(m/s) with resolution of 17.4×10^{-3} m/s.

In addition to the peak wavelength shifting analysis carried out for peak P1, other methods of output measurement can be used to describe the sensor behavior. The tracking of the intensity of the output power as

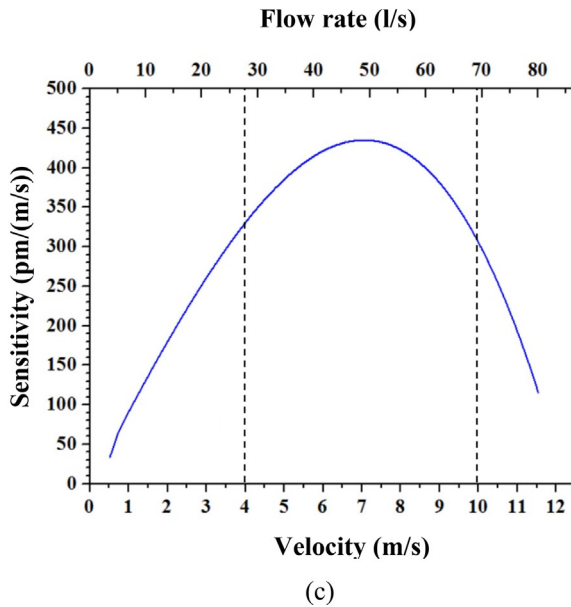
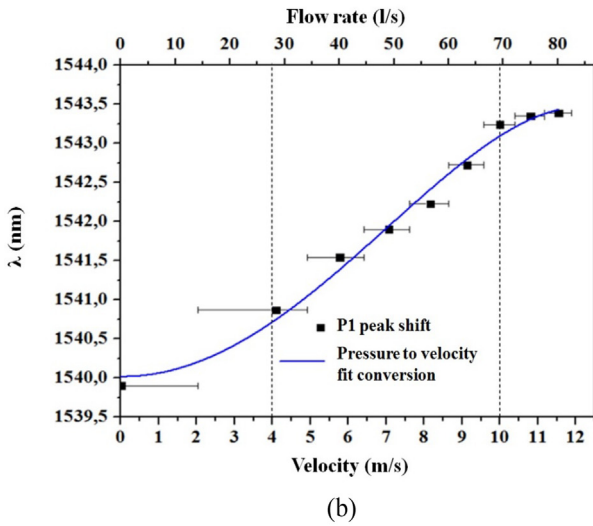
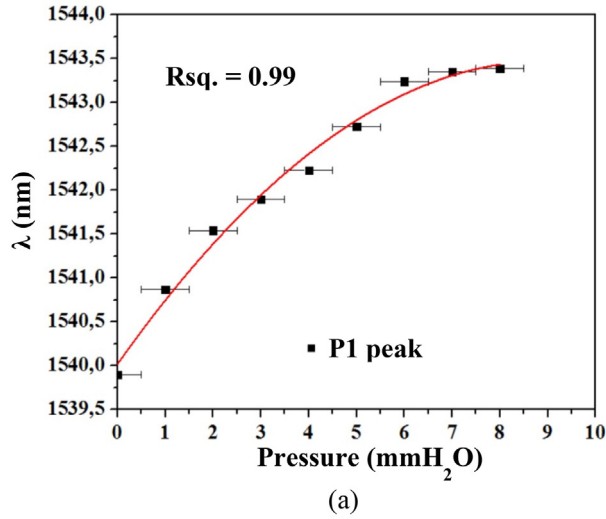


Fig. 7. (a) Wavelength shift of P1 peak as a function of the dynamic pressure with a polynomial fitting of order 2 as a solid line, (b) wavelength shift of P1 peak as a function of the air flow velocity and corresponding flow rate, using converted polynomial fitting and (c) sensitivity of the peak shifting.

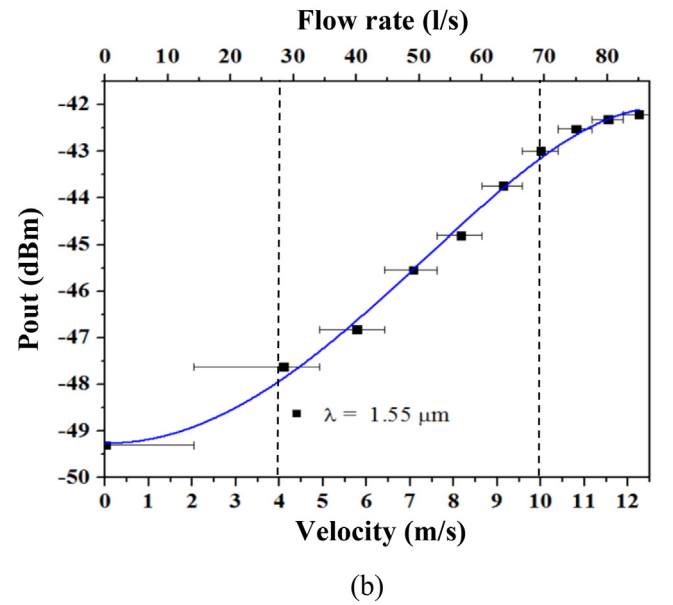
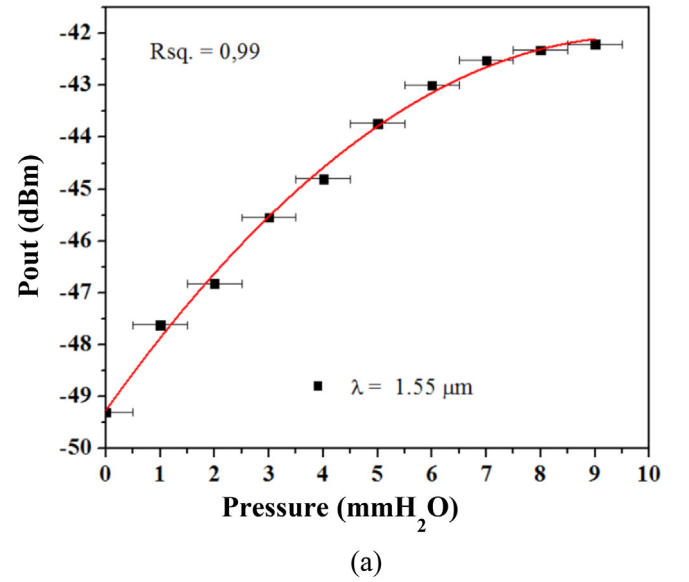
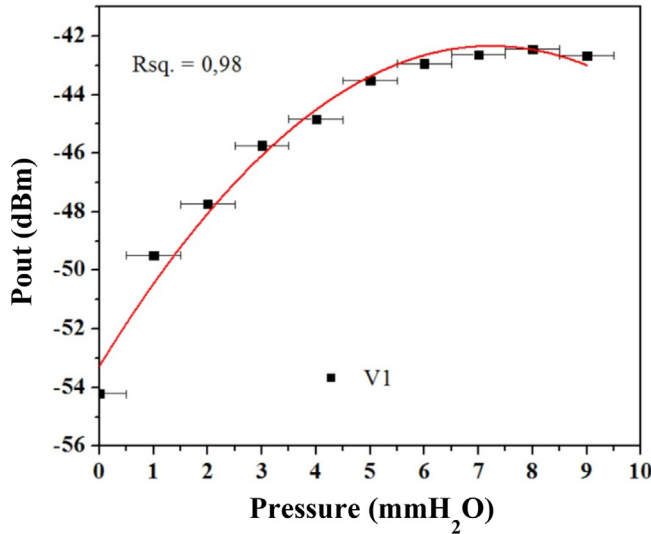


Fig. 8. (a) Output power for the fixed wavelength reference as a function of the dynamic pressure with a polynomial fitting of order 2 as a solid line and (b) output power as a function of the air flow velocity and corresponding flow rate using converted polynomial fitting.

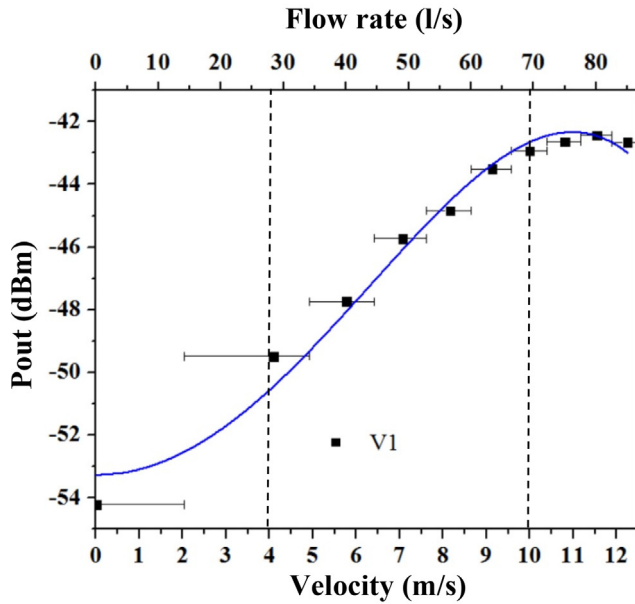
a function of pressure, velocity and flow rate was examined using the reflected spectra for a fixed wavelength value, for the valley V1 and a combination of the output power intensities for the peak P2 and the valley V1, as will be shown later in this section.

Using Eq. (3) and the experimental data given in Table 1, the self-image wavelength has a value of $\lambda = 1.55 \mu\text{m}$, which is used as the reference wavelength to examine the output power in the case of fixed wavelength value method. Fig. 8(a) shows the output power for the reference wavelength as a function of the dynamic pressure. A polynomial fit of order 2 is shown as a solid line. Fig. 8(b) shows the output power as a function of the air flow velocity and the corresponding air flow rate, converted using Eqs. (7), (8) and (9).

Fig. 9(a) shows the result of the data obtained by tracking the output power intensity changes for valley V1 as a function of the dynamic pressure. A polynomial fit of order 2 is shown as a solid line. Fig. 9(b) shows the same result of the output power as a function of the air flow velocity and the corresponding air flow rate, converted using



(a)



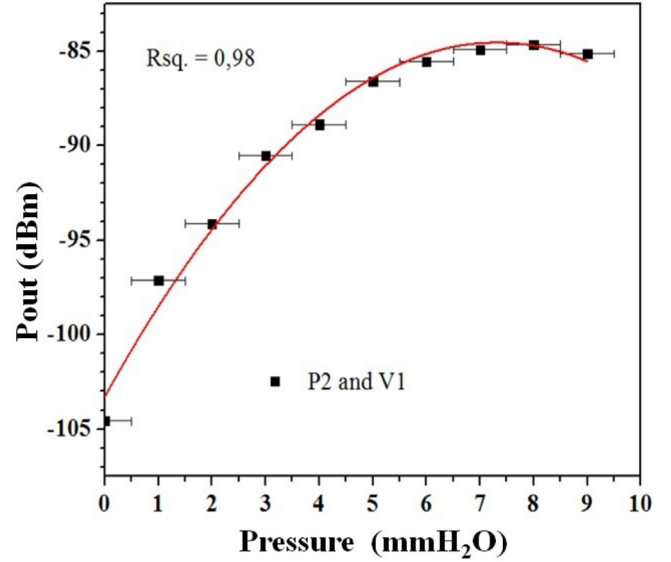
(b)

Fig. 9. (a) Output power for valley V1 as a function of the dynamic pressure with a polynomial fitting of order 2 as a solid line and (b) output power as a function of the air flow velocity and corresponding flow rate using converted polynomial fitting.

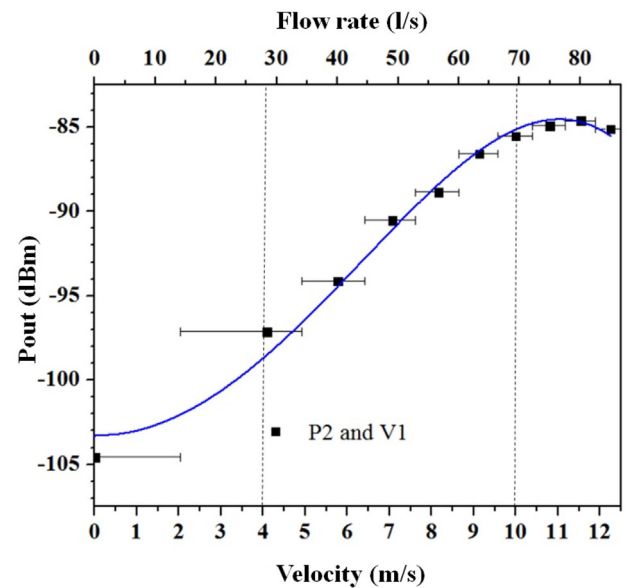
Eqs. (7), (8) and (9).

It is possible to reach higher values of sensitivity if we can track simultaneously peak P2 and valley V1 and combine them performing the addition of their output power in dBm. Fig. 10(a) shows, for P2 and V1 combination, the output power as a function of the dynamic pressure. A polynomial fit of order 2 is shown as a solid line. Fig. 10(b) shows the output power combination as a function of the air flow velocity and the corresponding air flow rate, converted using Eqs. (7)–(9). In order to make it easier to compare the sensor performance for the three last examination methods of measurement, Fig. 11 shows the sensitivity of the combination P2 and V1, the valley V1 and the chosen fixed wavelength $\lambda = 1.55 \mu\text{m}$ methods.

For the fixed wavelength, at the lower limit of 4 m/s and higher limit of 10 m/s the sensitivity is nearly 0.64 dB/(m/s) and 0.68 dB/(m/s), respectively. A peak sensitivity of 0.87 dB/(m/s) is achieved nearly the center of the chosen region (4 to 10 m/s), namely 7.38 m/s. At this



(a)



(b)

Fig. 10. (a) Output power of P2 and V1 combination as a function of the dynamic pressure with a polynomial fitting of order 2 as a solid line and (b) output power as a function of the air flow velocity and corresponding flow rate using converted polynomial fitting.

range the average sensitivity is 0.82 dB/(m/s). The examination of the valley V1 sensitivity curve shows that at the lower limit of 4 m/s and higher limit of 10 m/s the sensitivity is nearly 1.26 dB/(m/s) and 0.61 dB/(m/s), respectively. A peak sensitivity of 1.53 dB/(m/s) is obtained nearly the center of the chosen region, namely 6.35 m/s. At this range the average sensitivity is 1.37 dB/(m/s). For the P2 and V1 combination, at the lower limit of 4 m/s and higher limit of 10 m/s the sensitivity is nearly 2.14 dB/(m/s) and 1.10 dB/(m/s), respectively. A peak sensitivity of 2.62 dB/(m/s) is attained nearly the center of the chosen region, namely 6.37 m/s. At this range the average sensitivity is 2.35 dB/(m/s). In all methods the higher sensitivities are obtained around the center of the reliable range, nearly from 6 to 8 m/s. The use of P2 and V1 combination gives the highest sensitivity, almost three times the obtained with the fixed wavelength and nearly 1.7 times the obtained with V1, but on the other hand this advantage takes place at

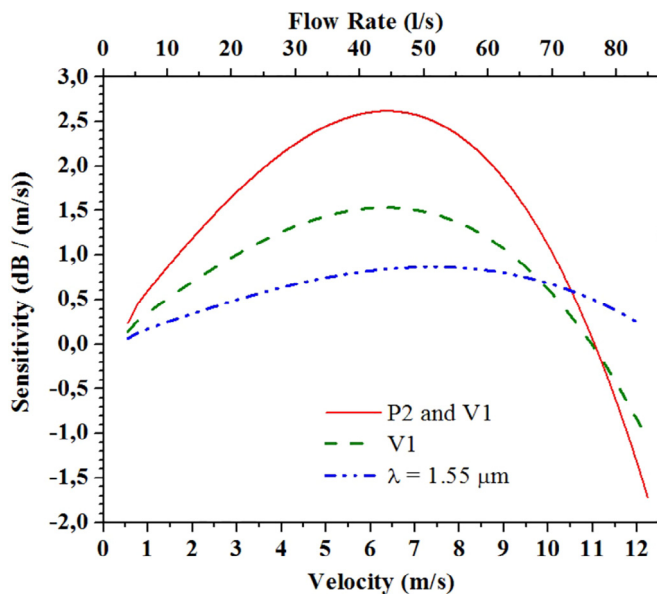


Fig. 11. Sensitivity for the combination P2 and V1 (red curve), the valley V1 (green curve) and the fixed wavelength $\lambda = 1.55 \mu\text{m}$ (blue curve) methods.

the expense of a more complex interrogation method. For very low velocity and flow rate applications, like in liquid dosing and chemical injection, the sensitivity of the sensor can be increased by adding a target, a circular flap for instance, at the tip of the sensor. As the deflection of the sensor increases with the target area, it can be used to control the sensitivity.

For the combination P2 and V1 and the valley V1 curves, Fig. 11 shows that negative sensitivity occurs nearly beyond 11 m/s, which corresponds to the slope inversion of the output power intensity curve in Figs. 9(b) and 10(b), respectively. It can be seen from Fig. 5 that the output power intensity curves for peak P2 and valley V1 have inversions of their behavior with velocity at the point 12.25 m/s, since its curve is located below the 11.55 m/s curve in the P2 and V1 region. It can occur to any isolated peak and valley output power response, depending on MMI results and field deformation as discussed in Section 3. Referring to the Fig. 2(b), as an example, it can be seen that there is a slope inversion nearly $R = 870 \text{ mm}$. On the left side of this point the output power intensity rises with the increase of the curvature radius (curvature lowering). On the right side the behavior is the opposite.

6. Conclusions

A fiber reflective sensor has been described and investigated. The MMF section is exposed to dragging forces on a fluid stream to bend, changing the MMI patterns and, therefore, the output light spectra. In the experimental tests air stream is used inside a wind tunnel providing a reliable dynamic range from 4 to 10 m/s. The sensor measurement can be made with a variety of interrogation techniques and the selection brings to a compromise among sensitivity and interrogation complexities. A peak sensitivity of $435.13 \text{ pm}/(\text{m/s})$ with resolution of $17.4 \times 10^{-3} \text{ m/s}$ is obtained using the wavelength shift of a chosen peak method. The measure of the output power intensity using a fixed wavelength is the simplest method and provided a peak sensitivity of $0.87 \text{ dB}/(\text{m/s})$. Tracking the output power of a single valley allowed to obtain a peak sensitivity of $1.53 \text{ dB}/(\text{m/s})$. Tracking a peak and a valley simultaneously and combine their output power is more complex, but generates much higher sensitivity, say $2.62 \text{ dB}/(\text{m/s})$. The best choice lies on the nature of the application. Inside a pipe, the sensor is naturally used as velocity and flow rate sensor. In free space it can be used as an anemometer or other important applications, such as stall detector for aerodynamic surfaces.

Acknowledgements

Authors acknowledge Prof. Maria Aparecida G. Martinez of CEFET-RJ, Prof. Cindy Stella Fernandes of UNIFESSPA-PA, Eng. Renato Trevisano Bellini of CEFET-RJ, Alberto Rubim da Cruz of LABFOT-IME-RJ, Msc. Hugo Eugênio de Freitas of Instituto de Física “Gleb Wataghin” – UNICAMP-SP, Prof. Marcelo Martins Werneck of UFRJ-RJ and Msc. Ariadny da Silva Arcas of UFRJ-RJ, for the partial support to this work.

Authors also would like to thank the Brazilian Funding Agencies CAPES and CNPq.

References

- [1] A. Mehta, W. Mohammed, E.G. Johnson, Multimode interference-based fiber-optic displacement sensor, *IEEE Photon. Technol. Lett.* 15 (2003) 1129–1131.
- [2] E.G.P. Pachon, M.A.R. Franco, C.M.B. Cordeiro, Spectral bandwidth analysis of high sensitivity refractive index sensor based on multimode interference fiber device, *Proc. SPIE* 8421 (2012) 84217Q-184217Q-4.
- [3] X. Zhou, K. Chen, X. Mao, W. Peng, Q. Yu, A reflective fiber-optic refractive index sensor based on multimode interference in a coreless silica fiber, *Opt. Commun.* 340 (2015) 50–55.
- [4] Q. Wang, G. Farrell, W. Yan, Investigation on single-mode-multimode-single-mode fiber structure, *IEEE J. Lightw. Technol.* 26 (2008) 512–519.
- [5] E. Li, X. Wang, C. Zhang, Fiber-optic temperature sensor based on interference of selective higher-order modes, *Appl. Phys. Lett.* 89 (2006) 091119-1–091119-3.
- [6] A. Kumar, R.K. Varshney, S.A. Cleitus, P. Sharma, Transmission characteristics of SMS fiber optic sensor, *Opt. Commun.* 219 (2003) 215–219.
- [7] C.S. Fernandes, M.T.M.R. Giraldo, M.J. Souza, J.C.W.A. Costa, C. Gouveia, P. Jorge, M.A.R. Franco, Curvature and vibration sensing based on Core Diameter Mismatch Structures, *IEEE Trans. Instrum. Meas.* 65 (2016) 2120–2128.
- [8] S.M. Tripathi, A. Kumar, R.K. Varshney, Y.B.P. Kumar, E. Marin, J.P. Meunier, Strain and temperature sensing characteristics of single-mode-multimode-single-mode structures, *J. Lightw. Technol.* 27 (2009) 2348–2356.
- [9] Q. Wu, M. Yang, J. Yuan, H.P. Chan, Y. Ma, Y. Semenova, P. Wang, C. Yu, G. Farrell, The use of a bend singlemode-multimode-singlemode (SMS) fibre structure for vibration sensing, *Opt. Laser Technol.* 63 (2014) 29–33.
- [10] H. Ahmad, S.N. Aidit, S.O. Ooi, Z.C. Tiu, Supercontinuum micrometer-displacement sensor using single-multi-air-gap-single mode fiber as sensing probe, *IEEE Sens. J.* 18 (2018) 8275–8279.
- [11] N.A. Ahmad, S.H. Dahlan, N.A. Cholan, H. Ahmad, I.S. Amiri, Z.C. Tiu, Dual-wavelength thulium fluoride fiber laser based on SMF-TMSIF-SMF interferometer as potential source for microwave generation in 100-GHz region, *IEEE J. Quantum Electron.* 54 (2018) 1–7.
- [12] H. Ahmad, S.I. Ooi, Z.C. Tiu, 100 GHz free spectral range-tunable multi-wavelength fiber laser using single-multi-single mode fiber interferometer, *Appl. Phys. B* 125 (99) (2019) 1–11.
- [13] A.S. Khan, M.S. Raean, An efficient wavelength variation approach for bend sensing in single mode-multimode-single mode optical fiber sensors, *Int. J. Adv. Comput. Res.* 2 (2012) 153–159.
- [14] R.M. Silva, M.S. Ferreira, J. Kobelke, K. Schuster, O. Frazão, Simultaneous measurement of curvature and strain using a suspended multicore fiber, *Opt. Lett.* 36 (2011) 3939–3941.
- [15] P. Wang, G. Brambilla, Y. Semenova, Q. Wu, G. Farrell, A simple ultrasensitive displacement sensor based on a high bend loss single-mode fibre and a ratiometric measurement system, *J. Opt.* 13 (2011) 5.
- [16] R. Kuntaraco, A. Hatt, Sekartedjo, C. Prastyanto, I. Mochtar, Experimental characterization of a load sensor based on singlemode – multimode – singlemode (SMS) fiber structure with a variation of the number of bends, *IPTEK J. Proc. Ser. 1* (2014) 2354–6026.
- [17] H. Efendioglu, A. Sahin, T. Iyldirim, K. Fidanboyulu, Design of Hetero-core Smart Fiber Optic Macrobend Sensors, in: 7th Int. Conf. Elect. and Electron. Eng. (ELECO), (2011) II-372-375.
- [18] L. Battista, S. Sciuto, A. Scorza, Preliminary evaluation of a fiber-optic sensor for flow measurements in pulmonary ventilators, in: IEEE International Symposium on Medical Measurements and Applications, Bari, (2011) 29–34.
- [19] E. Schena, P. Saccomandi, S. Silvestri, A high sensitivity fiber optic macro-bend based gas flow rate transducer for low flow rates: theory, working principle, and static calibration, *Rev. Sci. Instrum.* 84 (2013) 024301-1–024301-7.
- [20] V. Lien, F. Vollmer, Microfluidic flow rate detection based on integrated optical fiber cantilever, *Lab. Chip* 7 (2007) 1352–1356.
- [21] L. Yuan, J. Yang, Z. Liu, A Compact Fiber-Optic Flow Velocity Sensor Based on a Twin-Core Fiber Michelson Interferometer, *IEEE Sens. J.* 7 (2008) 1114–1117.
- [22] V. Krasovskii, I. Feofanov, P. Ivashkin, M. Kazaryan, A fiber-optic Doppler blood flow-velocity sensor, *St. Petersburg Polytech. Univ. J.: Phys. Math.* 3 (2017) 35–38.
- [23] R. Hu, X. Huang, A simple fiber-optic flowmeter based on bending loss, *IEEE Sens. J.* 12 (2009) 1952–1955.
- [24] A. Vijayan, V. Thakare, R. Karekar, R. Aiyyer, Optical fiber-based macrobend free air flow sensor using a hinge joint: a preliminary report, *Microw. Opt. Technol. Lett.* 10 (2008) 2543–2546.
- [25] W. Peng, G. Pickrell, J. Xu, Z. Huang, D. Kim, et al., Novel single-phase fiber optic flow sensor system, *Proc. SPIE* 5272 (2004) 223–229.
- [26] G. Liu, Q. Sheng, G. Piassetta, W. Hou, M. Han, A fiber-optic water flow sensor

- based on laser-heated silicon Fabry-Perot cavity, *Proc. SPIE* 9852 (2016).
- [27] G. Liu, W. Hou, W. Qiao, M. Han, Fast-response fiber-optic anemometer with temperature self-compensation, *Opt. Express* 23 (2015) 13562–13570.
- [28] Y. Zhao, K. Chen, J. Yang, Novel target type flowmeter based on a differential fiber Bragg grating sensor, *Measurement* 38 (2005) 230–235.
- [29] S. Thekkethil, R. Thomas, H. Neumann, R. Ramalingam, Experimental investigation on mass flow rate measurements using fibre Bragg grating sensors, *IOP Conf. Ser.: Mater. Sci. Eng.* 171 (2017) 8.
- [30] R. Lva, H. Zhenga, Y. Zhaoa, Y. Gua, An optical fiber sensor for simultaneous measurement of flow rate and temperature in the pipeline, *Opt. Fib. Technol.* 45 (2018) 313–318.
- [31] Q. Zhaoa, H. Zhenga, R. Lv, Y. Gua, Y. Zhao, Y. Yang, Novel integrated optical fiber sensor for temperature, pressure and flow measurement, *Sens. Actuat. A Phys.* 280 (2018) 68–75.
- [32] B. Dakić, J. Bajić, D. Stupar, M. Slankamenac, M. Živanov, A novel fiber-optic mass flow sensor, *Key Eng. Mater.* 543 (2013) 231–234.
- [33] S. Chewa, A. Zulkiflia, S. Masnanb, S. Akibc, S. Haruna, F. Adikana, H. Ahmad, Water wave gauge based on singlemode-multimode-singlemode fiber structure, *Optik* 144 (2017) 232–239.
- [34] J. Ang, S. Idapalapati, A. Asundi, Flow measurements using a simple fiber optic technique, *World Cong. Adv. Civ. Environ. Matter. Res. (ACEM' 12)* (2012) 26–30.
- [35] W. Mohammed, A. Mehta, E. Johnson, Wavelength tunable fiber lens based on multimode interference, *J. Light. Technol.* 22 (2004) 469–477.
- [36] L. Soldano, E. Pennings, Optical multi-mode interference devices based on self-imaging: principles and applications, *J. Light. Technol.* 13 (1995) 615–627.
- [37] D. Marcuse, Field deformation and loss caused by curvature of optical fibers, *J. Opt. Soc. Am.* 66 (1976) 311–320.
- [38] Y. Gong, T. Zhao, Y. Rao, Y. Wu, All-fiber curvature sensor based on multimode interference, *IEEE Photonics Technol. Lett.* 23 (2011) 679–681.
- [39] C. Caucheteur, K. Chah, F. Lhomme, M. Blondel, Patrice Megret, Simultaneous bend and temperature sensor using tilted FBG, *Proc. SPIE* 5855 (2005) 707–711.